

Coherent Nonlinear Optical Imaging: Beyond Fluorescence Microscopy

Wei Min,^{1,*} Christian W. Freudiger,^{1,2} Sijia Lu,¹
and X. Sunney Xie¹

¹Department of Chemistry and Chemical Biology, and ²Department of Physics, Harvard University, Cambridge, Massachusetts 02138; email: xie@chemistry.harvard.edu

*Current address: Department of Chemistry, Columbia University, New York, New York 10027

Annu. Rev. Phys. Chem. 2011. 62:507–30

The *Annual Review of Physical Chemistry* is online at
physchem.annualreviews.org

This article's doi:
10.1146/annurev.physchem.012809.103512

Copyright © 2011 by Annual Reviews.
All rights reserved

0066-426X/11/0505-0507\$20.00

Keywords

label-free imaging, coherent Raman spectroscopy, stimulated Raman scattering microscopy, stimulated emission microscopy, pump-probe microscopy

Abstract

The quest for ultrahigh detection sensitivity with spectroscopic contrasts other than fluorescence has led to various novel approaches to optical microscopy of biological systems. Coherent nonlinear optical imaging, especially the recently developed nonlinear dissipation microscopy (including stimulated Raman scattering and two-photon absorption) and pump-probe microscopy (including excited-state absorption, stimulated emission, and ground-state depletion), provides new image contrasts for nonfluorescent species. Thanks to the high-frequency modulation transfer scheme, these imaging techniques exhibit superb detection sensitivity. By directly interrogating vibrational and/or electronic energy levels of molecules, they offer high molecular specificity. Here we review the underlying principles and excitation and detection schemes, as well as exemplary biomedical applications of this emerging class of molecular imaging techniques.

INTRODUCTION

Modern optical microscopy is related intimately to molecular spectroscopy. Fundamentally speaking, various molecular spectroscopic transitions, linear or nonlinear, coherent or incoherent, can be used to provide distinct imaging contrast mechanisms for optical microscopy. As the underlying molecular spectroscopic and imaging scheme varies, the corresponding microscopy will exhibit different levels of detection sensitivity and provide contrast with different degrees of molecular selectivity.

Fluorescence spectroscopy (1) and microscopy (2), combined with the ever-expanding palette of genetically encoded fluorescent proteins (3–5), exogenous dyes, and semiconductor nanocrystals (6), are currently the most popular imaging contrasts used in biological studies. This is mainly because of the exquisite specificity given by the art of targeted probe labeling and the unprecedented sensitivity afforded by large electronic transition dipole moments and background-free fluorescence detection. As such, various fluorescence-based techniques have flourished, such as confocal laser scanning (2), two-photon excited fluorescence (7), single-molecule microscopy (8, 9), and super-resolution imaging (10).

However, many molecular species are intrinsically nonfluorescent or only weakly fluorescent. In addition, fluorescent labels, natural or artificial, are often perturbative, especially for small molecules such as signaling peptides, metabolites, neurotransmitters, and drugs, which are smaller than the fluorescent labels. Moreover, it is better not to use labeling or staining with fluorophores for *in vivo* medical applications on humans. Hence optical imaging methods with high sensitivity and specific molecular contrasts other than fluorescence are highly desirable in biomedical and materials science.

Coherent nonlinear molecular spectroscopy can generate a plethora of optical signals that do not rely on fluorescence emission, which is an incoherent process. Thus they offer contrast mechanisms for label-free chemical imaging. Depending on the underlying nonlinear optical processes, they can be grouped into the following three distinct categories:

1. Parametric generation spectroscopy, in which incident and resulting light fields exchange energy with each other while molecules remain in the ground state after nonlinear interaction. This includes second harmonic generation, third harmonic generation, four-wave-mixing processes, and coherent anti-Stokes Raman scattering (CARS).
2. Nonlinear dissipation optical spectroscopy, in which molecules exchange energy with incident laser fields (normally at two different wavelengths) after nonlinear interaction. This includes stimulated Raman scattering (SRS) and two-photon absorption.
3. Pump-probe spectroscopy, in which the pump pulse is used to excite molecules and the subsequent probe pulse is used to interrogate the transient states through excited-state absorption, stimulated emission, or ground-state depletion. In contrast to the above two categories, a certain time delay between the pump and probe pulses often is necessary to probe dynamic evolution of the molecular states.

Although parametric generation spectroscopy has been studied extensively and utilized for optical microscopy, the demonstration and application of nonlinear dissipation spectroscopy and pump-probe spectroscopy for chemical imaging have been explored only recently. Experimentally, nonlinear dissipation microscopy and pump-probe microscopy use femtosecond or picosecond mode-locked pulse trains, which have high peak power but low average power and can employ a similar high-frequency modulation transfer scheme to achieve high sensitivity (11). In addition, these two categories carry specific spectroscopic signatures by interrogating directly vibrational and/or electronic resonance energy levels of molecules.

A generic modulation transfer scheme for nonlinear dissipation microscopy and pump-probe microscopy is depicted in **Figure 1**. First, two temporally synchronized ultrafast laser pulse trains (pump and probe) are combined spatially and are focused collinearly onto a common focal spot in the sample. Second, before reaching the sample, the intensity (and, in principle, other quantities such as frequency, phase, and polarization) of the pump beam is modulated at a high frequency f (>1 MHz), whereas the probe beam is originally unmodulated. After interacting with the sample at the common focal volume, only the intensity of the probe beam is collected and detected by a photodiode. The readout of the photodiode is then demodulated by a lock-in amplifier to extract

Lock-in amplifier: a type of amplifier that can extract a small signal with a known carrier wave from an extremely noisy environment

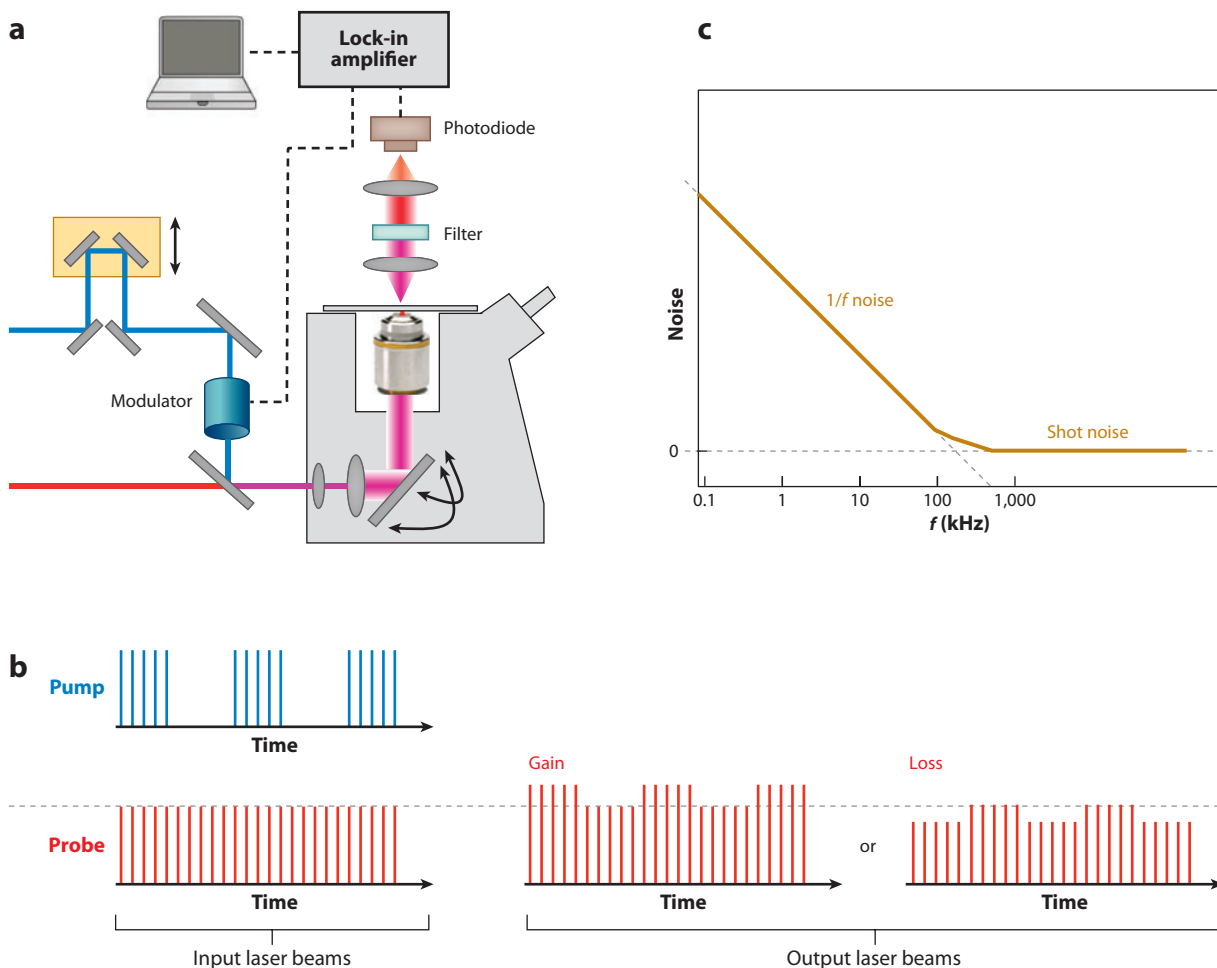


Figure 1

Principle of nonlinear dissipation microscopy and pump-probe microscopy in which a high-frequency modulation transfer scheme is utilized. (a) The generic experimental scheme. Both the pump and probe beams are focused onto a common focal spot with a microscope objective. The intensity (or frequency, polarization, phase, etc.) of the pump beam is modulated at a high frequency (>1 MHz), and the probe beam is collected and detected by a photodiode and then demodulated by a lock-in amplifier. (b) Temporal modulation behaviors of the input and output pump and probe pulse trains before and after nonlinear interaction with the sample. The probe beam could undergo either a gain or a loss in its intensity. (c) Noise spectrum of a typical laser source as a function of frequency f . In the low-frequency range (from DC to kilohertz), the noise follows the so-called $1/f$ noise. In the higher frequency, the noise approaches the flat floor of shot noise.

Table 1 Summary of physical properties of nonlinear dissipation microscopy and pump-probe microscopy and their desirable consequences in bioimaging

Properties	Consequences
No need for fluorescence	Imaging of nonfluorescent molecules
Targeting of electronic or vibrational states	Specificity given by molecular spectrum
High-frequency modulation/demodulation	Superb shot-noise-limited sensitivity
Overall nonlinear intensity dependence	Intrinsic 3D optical sectioning
Linear concentration dependence	Convenient quantification
Rapid modulation	No susceptibility to heterogeneous sample scattering

the modulation depth at the frequency f . Third, with the amount of the modulation transfer being registered for each pixel, a three-dimensional (3D) image then is constructed by scanning the combined pump/probe laser beams across the sample point by point with a laser scanning microscope.

The high frequency of f is crucial to achieve desirable imaging sensitivity. Laser intensity noise occurs primarily at low frequencies (from DC to kilohertz) in the form of the so-called $1/f$ noise, as shown in **Figure 1c**. As f goes above the megahertz range, the laser intensity noise gradually approaches the floor of quantum shot noise, which is always present because of the Poissonian distribution of the photon counts at the detector. Therefore, the narrow-band modulation/demodulation at f removes the low-frequency $1/f$ laser intensity noise and allows for shot-noise-limited detection sensitivity. Moreover, as the focused laser beam is scanned across the specimen, the intensity variation due to linear light scattering of heterogeneous biological samples will be filtered out by the high-frequency lock-in amplifier because those intensity variations occur at relatively slow scanning frequencies.

The same quantitative feature is shared by these modulation transfer techniques. Under the unsaturated condition, the signal strength, S , which is defined as the amount of intensity modulation generated to the originally unmodulated probe beam at the frequency f , is proportional to the product of the pump beam intensity, I_{pump} ; the probe beam intensity, I_{probe} ; the analyte concentration, $[c]$; and a specific molecular cross section of the analyte, σ_{molecule} , for the corresponding optical process:

$$S \propto [c] \cdot \sigma_{\text{molecule}} \cdot I_{\text{pump}} \cdot I_{\text{probe}}. \quad (1)$$

Because of the overall quadratic intensity dependence, the signal is generated only at the laser focus at which the optical intensity is the highest. Such a nonlinearity allows for 3D optical sectioning without the use of a confocal pinhole, similar to two-photon excited fluorescence microscopy (7). This is also the reason why these techniques are categorized as nonlinear optical microscopy. In addition, the linear concentration dependence of the analyte permits straightforward quantification, as opposed to parametric generation microscopy, which often exhibits quadratic concentration dependence. **Table 1** summarizes the important physical properties and the resulting desirable consequences of nonlinear dissipation microscopy and pump-probe microscopy in bioimaging practice.

PARAMETRIC GENERATION MICROSCOPY

In all parametric generation processes, a coherent radiation is generated at a color different from those of the incident laser beams, making it easy to detect by spectral separation. Hence this is the category that has been studied most extensively. Among the techniques, second harmonic

(Optical) shot noise: intrinsic statistical uncertainty of the measured light intensity due to the Poissonian distribution of photon counts within a certain time window

generation (12–14), third harmonic generation (15, 16) and four-wave-mixing (17–19) microscopy utilize nonlinear electronic polarization of the molecules under laser pulse excitation. In particular, second harmonic generation, which is sensitive to molecular symmetry breaking, has found useful applications in a number of biological systems, such as imaging collagen distribution (20, 21) and the detection of membrane potentials (14). However, because no real vibrational or electronic quantum states of the molecules are probed directly, there is limited information about the internal molecular identity in these contrast mechanisms.

Another nonlinear parametric generation process is CARS (22), which probes the vibrational states of molecules and is related intimately to spontaneous Raman scattering. Because spontaneous Raman cross sections are typically $10 \sim 12$ orders of magnitude smaller than the absorption cross section, spontaneous Raman microscopy often requires very long acquisition times (23). In addition, the unavoidable autofluorescence background of biological specimens often overwhelms the feeble spontaneous Raman signal from the target chemical species. As a third-order nonlinear Raman process, however, CARS can circumvent the feebleness of spontaneous Raman scattering by detecting the vibrational coherence of an ensemble of molecules within the laser focus (11, 22, 24, 25). In brief, when the energy difference, Ω , between the pump and probe (also called the Stokes beam in the Raman literature) matches the energy gap, ω_v , of a particular vibrational transition, $\Omega \equiv \omega_{\text{pump}} - \omega_{\text{probe}} \rightarrow \omega_v$, then the (difference frequency) beating between the pump and probe beams drives the vibrational oscillators within the focus coherently in phase. As shown in **Figure 2a**, the resulting vibrational coherence (i.e., ρ_{vib} , the off-diagonal element of the density matrix characterizing the degree to which the molecules in the ensemble oscillate in unison) is further read out by additional scattering off the pump beam to generate a coherent radiation at the anti-Stokes frequency $\omega_{\text{as}} = 2\omega_{\text{pump}} - \omega_{\text{probe}}$.

Quantitatively, the ratio between resonant CARS and spontaneous Raman emission radiation rates, $r_{\text{CARS}}/r_{\text{spont.Raman}}$, is approximately proportional to the number of vibrational oscillators, N , in the excitation volume and the square of the coherence amplitude, ρ_{vib} : $r_{\text{CARS}}/r_{\text{spont.Raman}} \approx N \cdot |\rho_{\text{vib}}|^2$ (26, 27). A crude estimate of the coherence follows $\rho_{\text{vib}} \approx \Xi_{\text{pump}} \cdot \Xi_{\text{probe}} \cdot \tau / \Delta$, where $\Xi_{\text{pump,probe}}$ is the Rabi frequency of the pump or probe field, respectively; τ is the pulse length; and Δ is the detuning from the electronic resonance. Whereas the intensity of incoherent emission of spontaneous Raman scattering is simply proportional to the number of incoherent emitters, the CARS fields produced by coherent emitters add up in amplitude first and then are squared to produce the intensity. Hence the CARS intensity is proportional to the square of the number of coherent emitters, which has been demonstrated in microscopy configurations experimentally (28). It is the constructive interference among all the coherent vibrational oscillators within the focus that gives rise to the amplification of the coherent radiation.

However, the CARS signal exists even when Ω is tuned off from all the vibrational resonance. Such a nonresonant background is actually a four-wave-mixing parametric generation process (11, 24, 25), as shown in **Figure 2b**, and is generated by the nonlinear electronic response of the sample mediated through virtual states. This background poses serious problems for CARS microscopy in two interrelated ways (29–31). First, as described by the last term of the following equation,

$$I_{\text{CARS}}(\Omega) \propto \left(\left| \chi_R^{(3)}(\Omega) \right|^2 + \left| \chi_{\text{NR}}^{(3)} \right|^2 + 2\chi_{\text{NR}}^{(3)} \text{Re} \left[\chi_R^{(3)}(\Omega) \right] \right) \cdot I_{\text{pump}}^2 \cdot I_{\text{probe}}, \quad (2)$$

the nonresonant background electric field distorts the CARS spectrum due to its constructive and destructive interference with the resonant vibrational contribution, $\text{Re}[\chi_R^{(3)}(\Omega)]$, on the low- and high-energy sides of the Raman peak, respectively (22). Such a spectral distortion effect results in a CARS spectrum that differs from the corresponding spontaneous Raman spectrum (as illustrated by **Figure 3a,b**), which is particularly problematic in the congested fingerprint region.

ρ_{vib} : off-diagonal element of the density matrix characterizing the coherence between the ground vibrational state and the first excited vibrational state, and the degree to which the molecules in the ensemble oscillate in unison

Nonresonant CARS background:

a four-wave-mixing parametric process generated by the nonlinear electronic response of the sample mediated through virtual states

Virtual state:

a short-lived intermediate quantum state that mediates otherwise forbidden transitions in a multistep process

$\chi^{(3)}$: third-order polarizability that describes the nonlinear tendency of the charge distribution of a molecule to be distorted by an external strong electric field

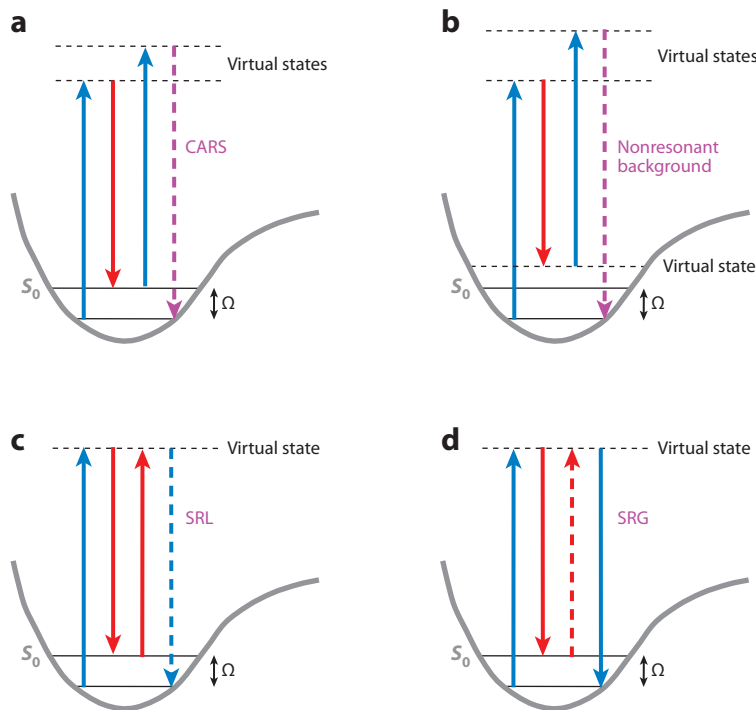


Figure 2

Energy-level diagrams of different third-order nonlinear induced polarizations. (a) When the energy difference between the pump and probe beams is resonant with a vibrational transition of the molecule, a strong resonant coherent anti-Stokes Raman scattering (CARS) signal at the anti-Stokes frequency is emitted. (b) When the energy difference between the pump and probe beams is not resonant with any vibrational transitions of the material, a weak but nonvanishing signal, known as the nonresonant background, is still generated at the anti-Stokes frequency. (c) The stimulated Raman loss (SRL) occurring at the pump field frequency has the opposite (180° lag) phase compared with the pump field. (d) The stimulated Raman gain (SRG) occurring at the probe field frequency has the same (0° lag) phase as that of the probe field.

Second, the nonresonant background limits the detection sensitivity of CARS microscopy. In the scenario of dilute analytes, $|\chi_R^{(3)}(\Omega)|^2 \ll |\chi_{NR}^{(3)}|^2$, and Equation 2 simplifies to $I_{CARS}(\Omega) \propto |\chi_{NR}^{(3)}|^2 + 2\chi_{NR}^{(3)}\text{Re}[\chi_R^{(3)}(\Omega)]$. The signal-to-noise ratio of CARS detection then becomes

$$SNR_{CARS} \propto \frac{2\chi_{NR}^{(3)}\text{Re}[\chi_R^{(3)}(\Omega)] \cdot I_{pump}^2 \cdot I_{probe}}{\alpha \cdot |\chi_{NR}^{(3)}|^2 \cdot I_{pump}^2 \cdot I_{probe} + \chi_{NR}^{(3)} \cdot I_{pump} \cdot \sqrt{I_{probe}}} \xrightarrow{\alpha \rightarrow 0} 2\text{Re}[\chi_R^{(3)}(\Omega)] \cdot I_{pump} \cdot \sqrt{I_{probe}}, \quad (3)$$

where $\alpha \cdot |\chi_{NR}^{(3)}|^2 \cdot I_{pump}^2 \cdot I_{probe}$ denotes the low-frequency intensity noise carried by the nonresonant background due to the $1/f$ noise of the excitation lasers, and $\chi_{NR}^{(3)} \cdot I_{pump} \cdot \sqrt{I_{probe}}$ is the shot noise of the nonresonant background. The shot-noise limit is reached only in the ideal situation in which α is vanishing, $SNR_{CARS} \rightarrow 2\text{Re}[\chi_R^{(3)}(\Omega)] \cdot I_{pump} \cdot \sqrt{I_{probe}}$.

The first CARS microscope was reported in 1982 (32). The noncollinear geometry used did not allow 3D imaging, and the visible dye laser employed generated a large nonresonant background via two-photon electronic resonance, which overwhelmed the vibrationally resonant signals. Because

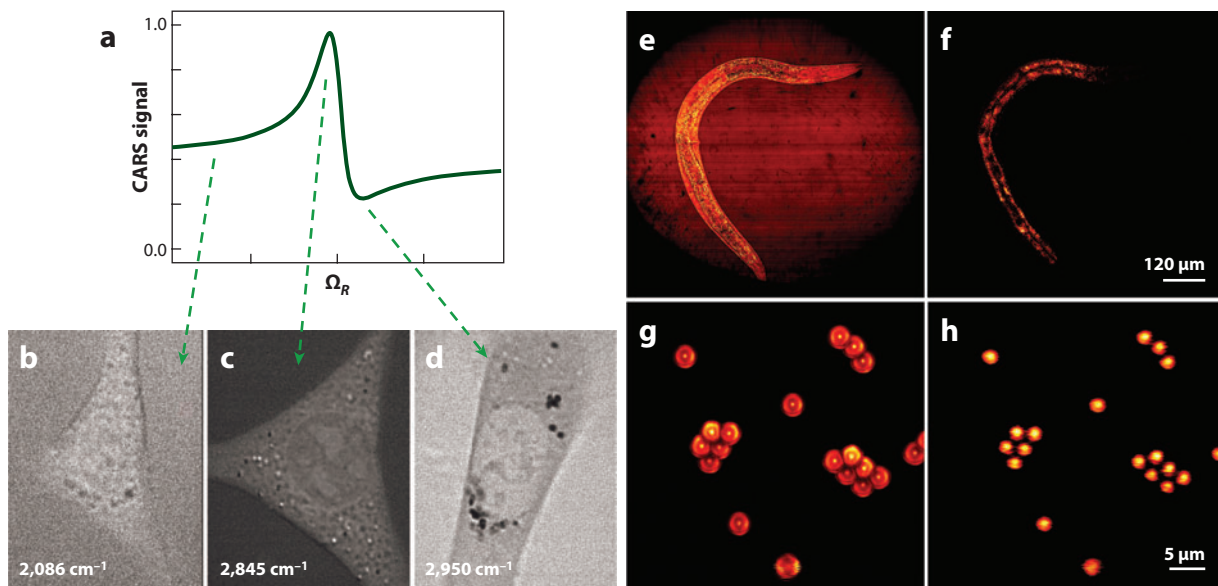


Figure 3

Comparison between coherent anti-Stokes Raman scattering (CARS) and stimulated Raman scattering (SRS) imaging. (a) The theoretical CARS spectrum resulting from interference between the nonresonant background and the real part of the vibrational resonant contribution. (b–d) Forward CARS images of 3T3-L1 cells tuned across the C–H resonance: (b) cell imaged at the C–H off-resonant condition (2,086 cm^{-1}), (c) cell imaged at the C–H resonant condition (2,845 cm^{-1}), and (d) cell imaged at the blue dip of the C–H band at 2,950 cm^{-1} . Resonant features appear dark against the nonresonant background. Panels b–d adapted from Reference 31. Simultaneous (e) epi-CARS and (f) SRS images of a live worm, *Caenorhabditis elegans*, with the Raman shift set to the lipid band at 2,845 cm^{-1} . Whereas SRS specifically probes the lipid contribution, the CARS contrast is complicated evidently by the nonresonant background from nonlipid structures. Simultaneous (g) epi-CARS and (h) SRS images of a layer of 2- μm polystyrene beads spin-coated on a glass coverslip, with the Raman shift at 2,845 cm^{-1} . Whereas the SRS image shows well-behaved round disks for single beads, the corresponding CARS images show a bright ring due to the interference effect occurring at the edge and a bright spot at the center due to the forward-going CARS signal being reflected back by the bead/air interface.

of these difficulties, the technique was not adopted for a long time. In 1999, 3D CARS imaging of living cells was achieved (33) by tightly focusing collinear pump and Stokes beams, which allowed 3D sectioning, and a near-infrared laser system was employed to suppress the nonresonant background. This work triggered rapid developments and widespread activities.

As it is a parametric generation process, CARS needs to satisfy the phase-matching condition, which is a consequence of the conservation of momentum. In conventional spectroscopy experiments as well as in early microscopy work (32), the CARS signal was detected in the phase-matching direction. Under the tightly focusing condition for microscopy, however, the large cone angle of the k vectors of the pump and Stokes beams relaxes the phase-matching condition (33). As a result, the CARS signal generated has a large cone angle of the k vector as well, even in the backward direction for an object with a size comparable with or smaller than the CARS wavelength, or for an interface between two media with different $\chi^{(3)}$ (29, 34). This results from the constructive and destructive interference of CARS radiation from different parts of the sample. Hence the CARS image has a complicated dependence on the exact object geometry. Image deconvolution with a point spread function, as is employed often in fluorescence microscopy, is no longer possible. An example is shown in **Figure 3g** for an individual polymer bead that exhibits a donut-like shape in the backward direction. The forward and backward images are not the same. This complication

k vector: a vector with its magnitude inversely proportional to the wavelength and its direction parallel to the direction of wave propagation

by such a spatial coherence effect makes the interpretation of CARS images difficult unless prior knowledge of the object's exact geometry is available.

We note that another mechanism for a CARS signal detected in the backward direction is the forward-going CARS signal being reflected backward by scattering after the focal plane, which explains the observed dot at the center of each bead in **Figure 3g**. The backward-reflected CARS in highly scattering tissue samples is strong enough to allow one to record CARS movies on live animals with video rate (~ 30 frames per second) (35). A major application of CARS microscopy in biomedicine has been in imaging the structure and dynamics of lipids, which have abundant C-H stretching oscillators with a spectrally isolated Raman band. Applications have been reported at various levels, including the cell (36), the tissue (37, 38), and the organism (39, 40).

In the past decade, numerous methods have been developed to suppress or circumvent the non-resonant background, including epi-detection (29, 34), polarization CARS (41, 42), time-resolved CARS (43), interferometric or heterodyne CARS (44–49), femtosecond pulse shaping (50–53), phase-retrieval CARS (54, 55), and frequency modulation CARS (56, 57). These methods have demonstrated varying degrees of success in the removal of the nonresonant background and the simplification of image interpretation. However, most were hampered by an increased complexity of instrumentation and data analysis. With the exception of interferometric CARS, all these methods still cannot resolve the complication due to phase matching and spatial coherence. Moreover, in spatially heterogeneous biological samples, phase- or polarization-sensitive imaging methods are limited ultimately in their sensitivity by variations of the refractive index and birefringence.

NONLINEAR DISSIPATION MICROSCOPY

The phenomenon of SRS was discovered immediately after the laser was invented (58–60). When a cell filled with nitrobenzene was introduced into a ruby laser cavity, Woodbury & Ng (58) observed a rather strong emission at a wavelength different than the fundamental wavelength of ruby laser, which was understood later as stimulated Raman gain. Two years later, a related phenomenon, stimulated Raman loss (or inverse Raman), was also discovered (59). Since then, stimulated Raman spectroscopy has been performed on various physical and chemical systems (61–63). In particular, femtosecond stimulated Raman spectroscopy has been developed to provide vibrational structural information with both high temporal and spectral information of chromophore systems such as primary photoisomerization and green fluorescent protein (64, 65).

SRS probes the excited vibrational population instead of the vibrational coherence detected by CARS (11, 25, 60). When Ω is tuned into a vibrational resonance, $\Omega \rightarrow \omega_v$, owing to the combined interaction of the incident pump and probe beams, the rate of the vibrational excitation is accelerated greatly compared with that in spontaneous Raman scattering by a factor given by

$$\frac{r_{stim.Raman}}{r_{spont.Raman}} = n_{probe} + 1, \quad (4)$$

where n_{probe} is the (normally large) number of photons in the optical mode of the probe beam (25). Such efficient excitation of a molecular vibrational level obviously requires energy input from the laser fields. As required by the law of energy conservation, each quantum of the vibrational excitation being excited is accompanied by one photon being annihilated in the pump beam and simultaneously one photon being created in the probe beam (**Figure 4a**). The resulting intensity loss in the pump beam is called stimulated Raman loss, and the intensity gain in the probe beam is called stimulated Raman gain.

Stimulated Raman gain and loss can be understood also in the semiclassical framework of nonlinear induced polarization (60) as an optical heterodyne phenomenon. When $\Omega \rightarrow \omega_v$, along

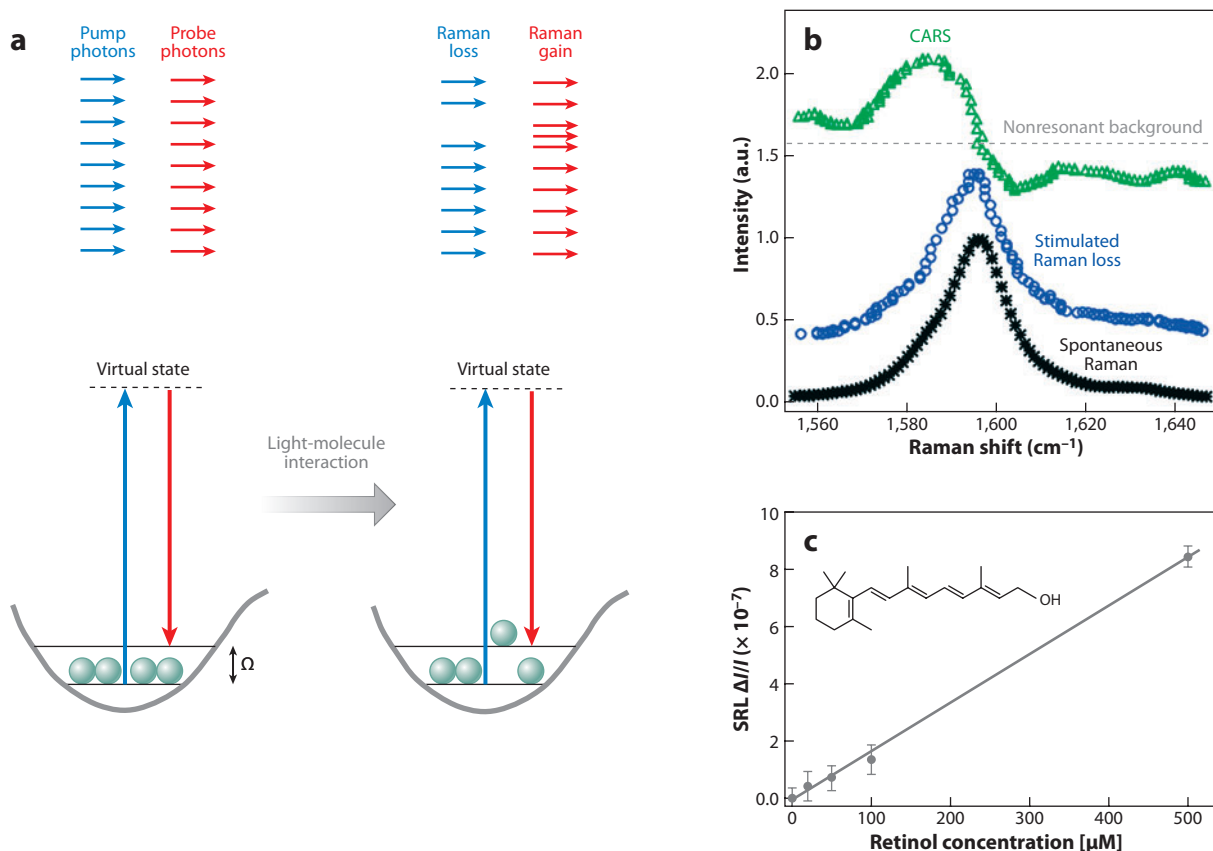


Figure 4

Principle of stimulated Raman scattering (SRS) microscopy. (a) Energy diagram of SRS when the energy difference between the pump and probe beams is resonant with a vibrational transition. Also depicted are the stimulated Raman gain (SRG) of the probe beam and stimulated Raman loss (SRL) of the pump beam after interaction with the vibrational oscillators. (b) Recorded spectra of the 1,595-cm⁻¹ Raman peak of 10-mM retinol in ethanol by spontaneous Raman scattering, coherent anti-Stokes Raman scattering (CARS), and SRS. Whereas the distorted CARS spectrum exhibits a typical peak shift, dispersive shape, and nonresonant background, the SRS spectrum is identical to the spontaneous Raman scattering spectrum. (c) The linear dependence of the SRS signal on concentrations of retinol in ethanol at 1,595 cm⁻¹. A modulation depth of $\Delta I_p/I_p < 10^{-7}$ can be detected. The detection limit was determined to be 50 μM.

with the CARS radiation at the anti-Stokes frequency, two other third-order induced polarizations, p_{pump} and p_{probe} , are generated at the fundamental pump and probe frequencies, shown in **Figure 2c,d**, respectively: $p_{\text{pump}} \propto \chi_R^{(3)}(\Omega) \cdot E_{\text{pump}} \cdot E_{\text{probe}}^2$ and $p_{\text{probe}} \propto \chi_R^{(3)}(\Omega) \cdot E_{\text{probe}} \cdot E_{\text{pump}}^2$. p_{pump} and p_{probe} propagate in the forward direction and interfere with the incident pump and probe fields with their corresponding phases. For stimulated Raman gain, p_{probe} interferes constructively with E_{probe} and results in an intensity gain:

$$\text{Gain}_{\text{probe}} = 2 \cdot p_{\text{probe}} \cdot E_{\text{probe}} \propto 2 \operatorname{Im} [\chi_R^{(3)}(\Omega)] \cdot I_{\text{probe}} \cdot I_{\text{pump}}. \quad (5)$$

For stimulated Raman loss, p_{pump} interferes destructively with E_{pump} and results in an intensity loss:

$$\text{Loss}_{\text{pump}} = -2 \cdot p_{\text{pump}} \cdot E_{\text{pump}} \propto -2 \operatorname{Im} [\chi_R^{(3)}(\Omega)] \cdot I_{\text{probe}} \cdot I_{\text{pump}}. \quad (6)$$

Such an optical heterodyne interpretation is analogous to the view that linear absorption can be treated as the destructive interference between the incident field and linear induced polarization of the molecule at the forward detector.

SRS as a contrast mechanism for microscopy was reported first in 2007 using multiplex detection with a photodiode array in combination with a femtosecond amplified laser system (66). Although the amplified laser system used generates a large SRS signal, it is not suitable for bioimaging because the excessive peak power causes sample damage and the low repetition rate limits the image acquisition speed. Our group overcame these problems using the combination of narrow-band high-repetition-rate picosecond pulse trains and high-frequency modulation transfer, which yielded superior sensitivity and fast imaging speed. We first demonstrated such SRS microscopy in 2008 (67), which was followed immediately by reports from two other groups in 2009 (68, 69).

SRS imaging is free from the nonresonant background in CARS microscopy. **Figure 3f** shows a simultaneous SRS CH_2 image of the same worm sample in **Figure 3e**. Only purely lipid contrast is visible in SRS because, in the absence of a vibrational eigenstate that could hold the population and energy, energy simply cannot transfer from the pump beam to the probe beam, as required by the law of energy conservation. In the optical heterodyne picture, the off-resonant polarization fields are either 90° ahead or 90° behind the incident pump or probe fields at the detector, which forbids the occurrence of any constructive or destructive interference (and hence intensity gain or loss) with the pump or probe beams.

Such a drastic contrast between SRS and CARS is analogous to the more familiar relation between absorption and Rayleigh scattering. Whereas a molecule's linear absorption can be tuned off completely from its absorption band, Rayleigh scattering always occurs, even if there is no resonance between the light and the molecule. Physically, scattering events can be mediated by a virtual state, whereas absorption events cannot. To some extent, SRS and CARS can be viewed as nonlinear Raman analogs of the linear absorption and Rayleigh scattering phenomena, respectively.

SRS overcomes all major difficulties associated with CARS microscopy, as summarized in **Table 2**. First, the absence of a nonresonant background eliminates the biggest obstacle for CARS imaging quantification and interpretation. Second, without the interference effect from the background, the SRS spectrum is identical to that of spontaneous Raman scattering (**Figure 4b**), allowing the straightforward utilization of all the accumulated knowledge of Raman spectroscopy. Third, the detection sensitivity of SRS is demonstrated to be much higher than that of CARS

Table 2 Comparison of spectroscopy and microscopy aspects between coherent anti-Stokes Raman scattering and stimulated Raman scattering imaging

Coherent anti-Stokes Raman scattering	Stimulated Raman scattering
Parametric generation process	Energy transfer process
Existence of nonresonant background	Absence of nonresonant background
Distorted complex spectrum	Identical spectrum to Raman scattering
Limitation of laser intensity noise	Shot-noise-limited sensitivity
Linear to quadratic concentration dependence	Linear concentration dependence
Complication of spatial coherence	Absence of spatial coherence
Nonexistence of point spread function	Existence of point spread function
Contamination by two-photon fluorescence	No susceptibility to background fluorescence

microscopy. The signal-to-noise ratio of SRS detection may be written as

$$SNR_{SRS} = \frac{2 \operatorname{Im} [\chi_R^{(3)}(\Omega)] \cdot I_{pump} \cdot I_{probe}}{\alpha \cdot I_{probe} + \sqrt{I_{probe}}} \xrightarrow{\alpha \rightarrow 0} 2 \operatorname{Im} [\chi_R^{(3)}(\Omega)] \cdot I_{pump} \cdot \sqrt{I_{probe}}, \quad (7)$$

where $\alpha \cdot I_{probe}$ denotes the laser intensity noise of the probe beam, and $\sqrt{I_{probe}}$ is the shot noise of the probe beam intensity. Owing to the high-frequency modulation and lock-in detection at a high f , $\alpha \cdot I_{probe}$ can be removed readily in SRS detection. With $\alpha \rightarrow 0$, SRS can reach the shot-noise limit, with detectable $\Delta I_p/I_p$ approaching 10^{-8} within 1 s of acquisition time.

It is worth noting that, based on Equations 3 and 7, $SNR_{CARS}|_{\alpha \rightarrow 0}$ is approximately equal to $SNR_{SRS}|_{\alpha \rightarrow 0}$ in the scenario in which laser intensity fluctuation can be eliminated completely and the shot noise (from the nonresonant background for CARS and from the probe beam for SRS) is the only remaining noise source. However, it is extremely hard for CARS to meet this ideal situation because of the difficulty of employing an effective high-frequency modulation technique. In CARS, when certain optical properties (e.g., frequency) of the pump or probe beam are modulated, the nonresonant background almost always leaves spurious intensity noise. In contrast, modulation transfer is easy to implement for SRS.

Moreover, SRS exhibits a few other favorable properties over CARS (**Table 2**). The concentration dependence of CARS turns over from a quadratic one in the high-concentration limit to a linear one in the limit of low analyte concentration (Equation 2), with the exact quantitative relation depending on the nonlinear nature of the surrounding solvent. In contrast, the strict linear concentration dependence of SRS permits straightforward and reliable quantification. In addition, because SRS involves measurements of the transmission differences of the input beams, it is phase matched automatically. Hence there exists a well-defined point spread function that can be used for image deconvolution (**Figure 3b**). Therefore, the image contrast in SRS microscopy is easy to understand because it is free from spatial coherence artifacts.

Although the phase-matching condition dictates that the SRS effect be detected by measuring the transmitted pump or Stokes beams in the forward direction, it is desirable to detect SRS in the backward direction for thick, nontransparent tissue samples as light does not penetrate them. Fortunately, this can be done if a large area detector is used to collect a significant portion of the backscattered light after the SRS signal is already generated at the laser focus (70).

Compared with spontaneous Raman microscopy, SRS exhibits an orders-of-magnitude faster imaging speed by virtue of optical amplification of the vibrational excitation rate. The photon energy dissipates into vibrational levels during both Raman processes, but with drastically different efficiency. As shown in Equation 4, the acceleration factor, $r_{stim.Raman}/r_{spont.Raman}$, could be estimated for the SRS imaging apparatus reported in Reference 67. 5-mM methanol, which corresponds to approximately 3×10^5 C-H vibrational oscillators within the laser focal volume, gives a stimulated Raman loss signal of approximately $\Delta I_{SRS}/I_p \sim 7 \times 10^{-8}$. With a known σ_{Raman} of approximately 10^{-29} cm² for one C-H bond, the total spontaneous Raman scattering cross sections of 3×10^5 C-H vibrational oscillators will add up to be 3×10^{-24} cm². Given that the laser waist area of a pump beam is 10^{-9} cm² under a tight focus, one would expect to produce a relative spontaneous Raman scattering signal with $\Delta I_{spont.Raman}/I_p = (3 \times 10^{-24} \text{ cm}^2)/(10^{-9} \text{ cm}^2) \sim 3 \times 10^{-15}$. Therefore, $r_{stim.Raman}/r_{spont.Raman}$ is estimated to be as high as $7 \times 10^{-8}/3 \times 10^{-15} \sim 10^7$, which accounts for the orders-of-magnitude acceleration of imaging speed so that video-rate SRS microscopy for live animal imaging becomes feasible (70).

Having achieved label-free vibrational specificity, unprecedented imaging speed, and superb detection sensitivity, SRS has opened up a wide range of chemical imaging applications in

Table 3 Vibrational bands and corresponding Raman shifts used in stimulated Raman scattering microscopy

Vibrational mode	Raman shift (cm ⁻¹)	Chemical(s)	Reference(s)
O-H stretching	~3,250	Water	71, 72
(C=)C-H stretching	~3,015	Unsaturated lipids	67
C-H ₃ stretching	~2,950	Proteins	67, 69
C-H ₂ stretching	~2,845	Saturated lipids	67
N-C=O stretching	~1,656	Proteins	68
Aryl ring stretching	~1,600	Lignin	73
Conjugated C=C stretching	~1,590	Retinoic acid	67
Asymmetric COC stretching	~1,100	Cellulose	73
O-P-O symmetric stretching	~1,095	Nucleic acid	72
Ring breathing of phenylalanine	~1,004	Proteins	72
S=O stretching	~670	DMSO	67

biomedical science and technology by targeting various vibrational bands (see **Table 3**). As shown in **Figure 5**, live cells can be imaged without external labeling by targeting directly different chemical moieties (67–69). Tissue pathologies (71) and food products (72) can be analyzed without the application of any dye staining. Reaction kinetics of biopolymer lignin under a chemical treatment can be imaged in situ with high spatial and temporal resolution (73). Small molecules such as drugs and metabolites can be monitored and followed inside tissue, as shown in **Figure 6**. The lipid storage of *Caenorhabditis elegans* and its genetic regulation can be explored in vivo when combined with genetic manipulation of this model organism (74). As illustrated in **Figure 3e,f**, unlike CARS microscopy, SRS probes only the lipid contribution from intestine and hypodermal without the nonresonant background contribution from other tissues, representing a major advantage for high-throughput genetic screening analysis.

Recently, we implemented a specially tailored excitation with broadband excitation pulses for SRS microscopy (75). With that we can probe specifically a molecular species with particular spectral features in the congested spectral regions in the presence of interfering species.

Another nonlinear dissipation coherent process is two-photon absorption. Historically, two-photon absorption was the first nonlinear quantum transition to be explored, having been predicted in 1931 by Goepfert-Mayer (76). The widely used two-photon excited fluorescence spectroscopy and microscopy (7) are based on the sensitive detection of the subsequent fluorescence emission following two-photon absorption by fluorophores. Two-photon absorption is a nearly simultaneous absorption of two low-energy photons in order to excite a molecule from one state (usually the ground state) to a higher-energy electronic state. The sum of the energies of the two photons is resonant with the energy difference between the lower and upper states of the molecule. It differs fundamentally from linear optical absorption in that the strength of absorption depends on the square of the light intensity, and the quantum mechanical selection rules are different.

Normally, two-photon absorption, as in two-photon excited fluorescence microscopy (7), is operated under a single-beam mode in which molecules are excited by an ultrafast (normally femtosecond or picosecond) pulse train from a mode-locked laser such as a titanium-sapphire laser. The two photons involved are drawn from the same laser beam and thus have similar frequencies within the laser pulse bandwidth. Hence it is difficult to distinguish these two photons spectrally with such a single-beam mode.

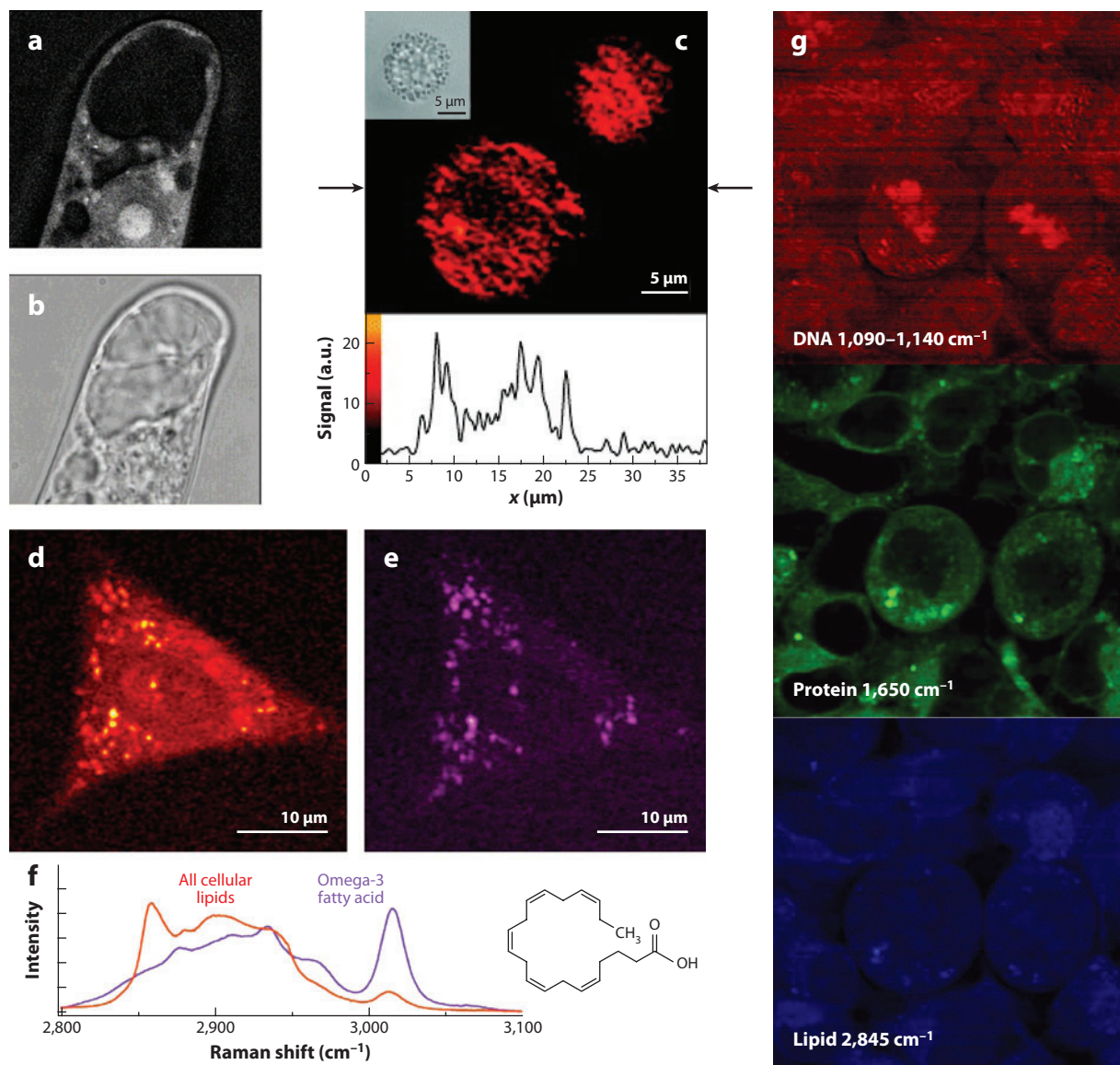


Figure 5

Stimulated Raman scattering (SRS) imaging of live cells at various spectral regions. (a) SRS image and (b) optical transmission micrograph of an unstained tobacco BY2 cultured cell with the Raman shift set to 2,967 cm^{-1} . The nucleus and cell walls of a tobacco BY2 cultured cell are visualized clearly. Panels *a* and *b* adapted from Reference 69. (c) SRS image of unstained human HL60 cells in an aqueous environment with the corresponding Raman shift being 1,659 cm^{-1} on resonance with the C=C stretching vibrations. Panel *c* adapted from Reference 68. (d,e) SRS images of a human lung cancer cell incubated with omega-3 fatty acids at 2,920 cm^{-1} and 3,015 cm^{-1} , respectively. A clear distinction of saturated and unsaturated lipid distributions is evident. (f) Spontaneous Raman spectra of oleic acid (with a single double C=C bond) and docosahexaenoic acid (with six double C=C bonds). The strong peak at 3,015 cm^{-1} is characteristic of unsaturated fatty acids. Panels *d–f* adapted from Reference 67. (g) Human embryonic kidney cells in metaphase, imaged at three different Raman shifts corresponding to DNA (1,090 ~ 1,140 cm^{-1}), protein (1,650 cm^{-1}), and lipid (2,845 cm^{-1}).

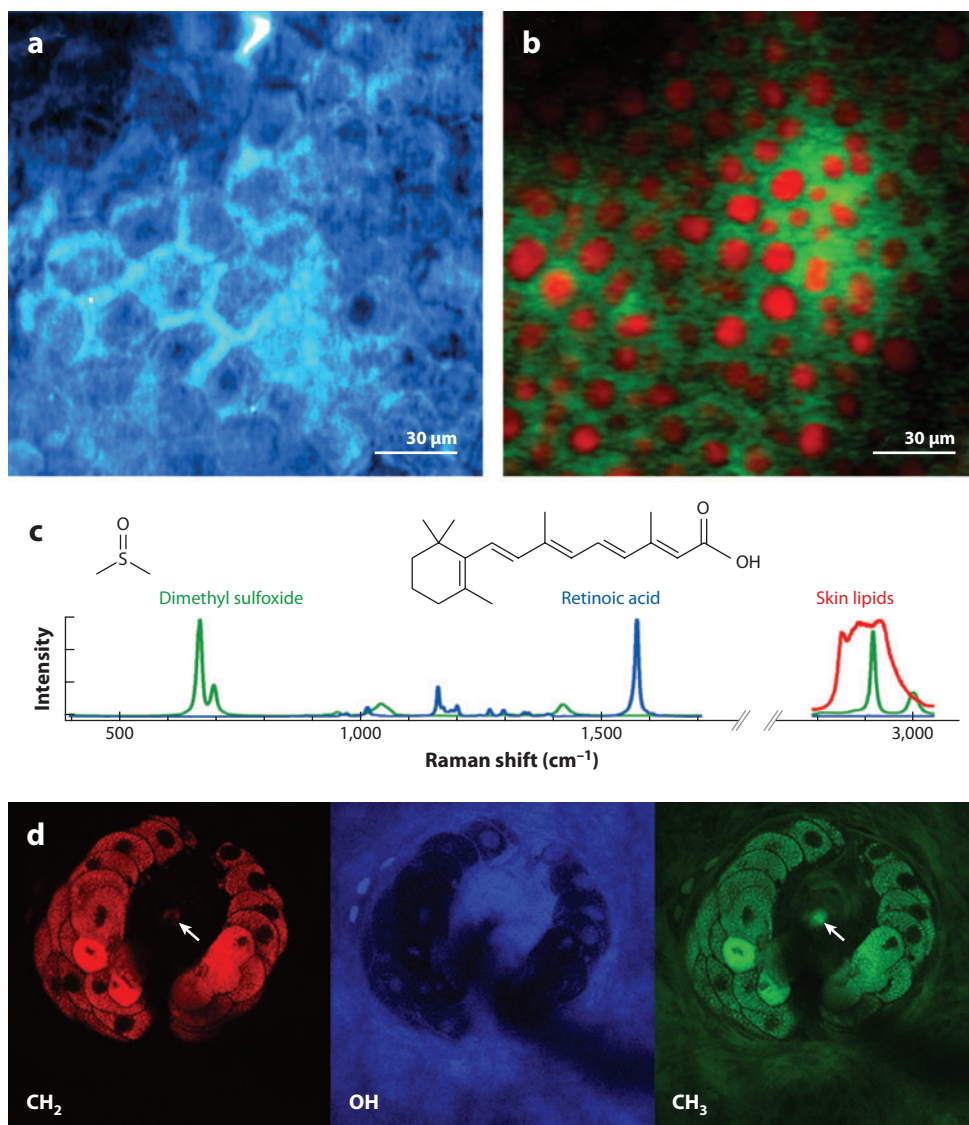


Figure 6

Tissue imaging by stimulated Raman scattering microscopy. Distributions of (*a*) topically applied compound retinoic acid and (*b*) penetration enhancer dimethyl sulfoxide (DMSO) in mouse ear skin. These images were acquired when tuned into the Raman shifts (*c*) of retinoic acid at 1,570 cm⁻¹ (blue) and DMSO at 670 cm⁻¹ (green). Skin structures are also highlighted by tuning into the CH₂ stretching vibration at 2,845 cm⁻¹ (red). Panels *a–c* adapted from Reference 67. (*d*) A sebaceous gland embedded in a mouse ear imaged at three different Raman shifts, corresponding to lipid CH₂, water OH, and protein CH₃. The arrows indicate a hair whose keratin is seen in the CH₃ image and oil coating in the CH₂ image. The subcellular resolution reveals the water-containing and lipid-deprived nuclei with reverse contrast.

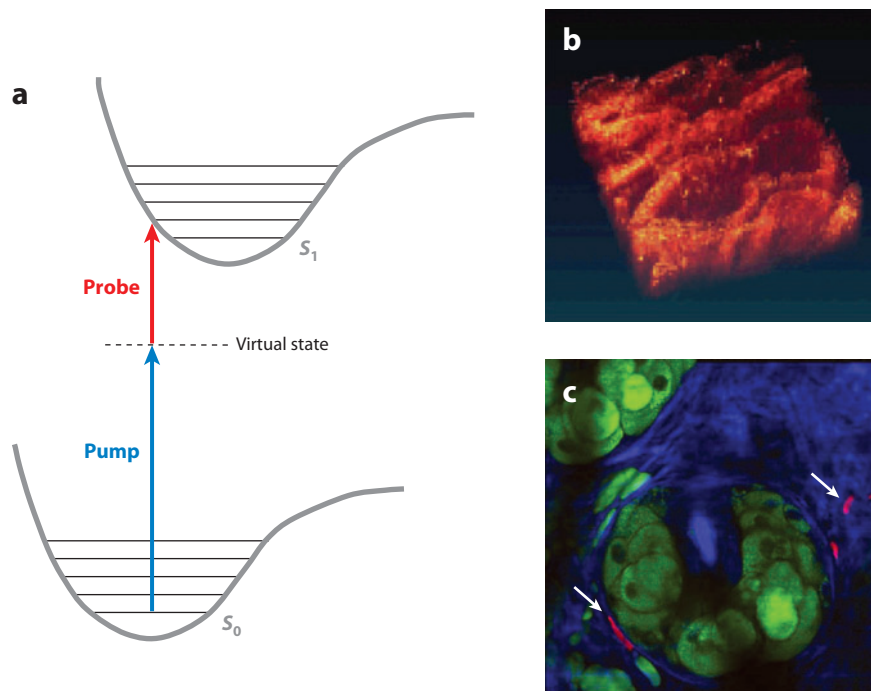


Figure 7

Two-photon absorption microscopy. (a) Energy diagram of simultaneous two-photon absorption by a high-lying electronic state through an intermediate virtual state. (b) 3D volume rendering of the two-photon absorption signal from human melanoma lesions obtained with femtosecond pulse trains of two different colors. Panel *b* adapted from Reference 78. (c) Two-photon absorption image of microcapillaries in a sebaceous gland of mouse skin with contrast due to hemoglobin in red blood cells (*magenta*). Overlaid are lipid (*green*) and protein (*blue*) stimulated Raman scattering images, taken with the same picosecond pulse trains, at corresponding Raman shifts, showing lipid-rich gland cells and adipocytes as well as protein-rich structures such as hairs and collagen, respectively.

Warren and coworkers (77, 78) first demonstrated the use of modulation transfer for two-photon absorption microscopy. In principle, two-photon absorption can be induced equally by two photons with different colors, as long as the sum of the energies of the two photons again matches the targeted electronic transition, the two laser pulse trains are temporally synchronized, and two laser beams are overlapped in space. In such a dual-beam mode, blocking the intensity of either color terminates the absorption of the other color by the molecules, as the successful absorption event necessitates the simultaneous presence of the two beams. Two-photon absorption microscopy provides contrast mechanisms for nonfluorescent chromophores that have appreciable two-photon absorption cross sections (77, 78), as shown in **Figure 7**. In the area of biomedicine, examples include beta-carotene, oxy-hemoglobin, deoxy-hemoglobin, melanin, and cytochromes.

Dual-beam two-photon absorption microscopy and SRS microscopy are related spectroscopically. They both operate through simultaneous two-photon transitions, with one photon drawn from the pump beam and one drawn from the probe beam, respectively, mediated through a virtual state. The difference is that, in the former, the probe photon continues to excite the molecule up to higher energy levels, whereas in the latter the probe photon brings the molecule down to the vibrationally excited state in the ground electronic manifold. In addition, the response functions

of two-photon absorption microscopy and SRS microscopy for a given molecule are given by the imaginary part of third-order nonlinear susceptibility (25). The difference lies in the fact that the former corresponds to two-photon resonance, whereas the latter is associated with the vibrational resonance.

PUMP-PROBE MICROSCOPY

Pump-probe spectroscopy has been widely used to study time-dependent ultrafast phenomena. In this section, we discuss its applications in chemical imaging: excited-state absorption microscopy, stimulated emission microscopy, and ground-state depletion microscopy.

Pump-probe microscopy was first reported for microscopy based on excited-state absorption by Warren's group using the modulation transfer technique (**Figure 8**). The pump and probe beams have to be in the form of ultrashort (a few hundred femtoseconds) pulse trains to interrogate effectively the transient excited states, as the excited lifetimes of those nonfluorescent chromophores are extremely brief (less than 1 ps). Hence the need for ultrashort pulses in pump-probe microscopy is fundamentally different from that in parametric generation microscopy or nonlinear dissipation microscopy. As a result, the pump and probe pulse trains do not need to overlap in time. In fact, the probe pulse train is delayed (by a few hundred femtoseconds) with respect to the pump pulse train to permit the molecule enough time to relax vibrationally on the electronic excited state.

Compared with two-photon absorption via an intermediate virtual state, excited-state absorption can enhance significantly the overall sensitivity by bringing a resonance between a real intermediate electronic state and the pump beam (79–81). For example, *ex vivo* and *in vivo* imaging of blood vessels in mouse ears have been demonstrated with dual-beam 775-nm and 650-nm excited-state absorption microscopy, by using the charge transfer absorption band of oxy-hemoglobin and deoxy-hemoglobin in the near infrared. Such an excited-state absorption imaging modality presents possibilities for oxygenation imaging based on differences in excited-state dynamics between oxy-hemoglobin and deoxy-hemoglobin (81).

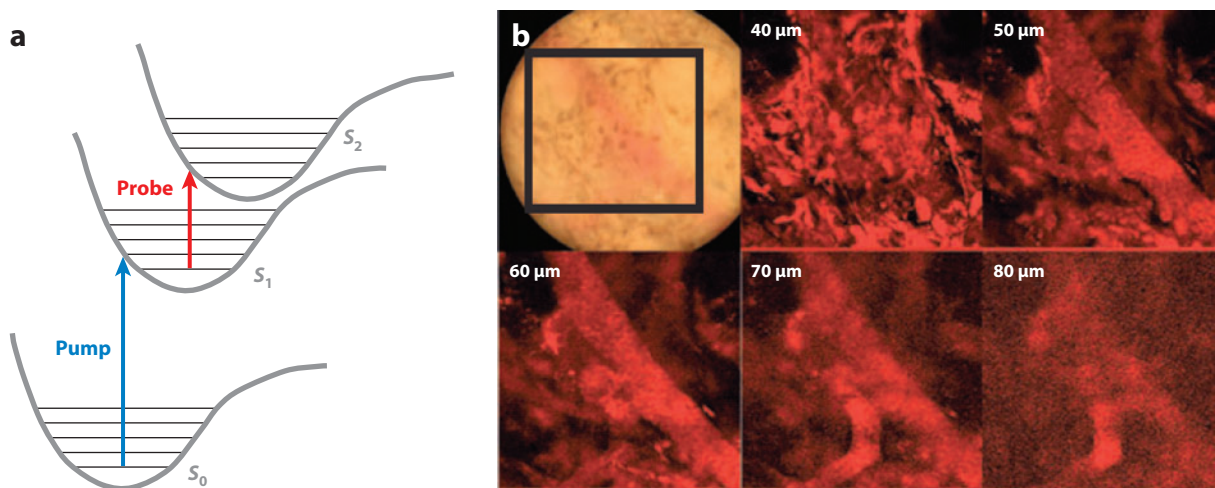


Figure 8

Excited-state absorption microscopy. (a) Energy diagram of sequential two-photon absorption via an intermediate electronic energy state. (b) Bright-field image and a series of laser scanning two-color excited-state absorption images from blood at various depths in a mouse ear. Figure adapted from Reference 79.

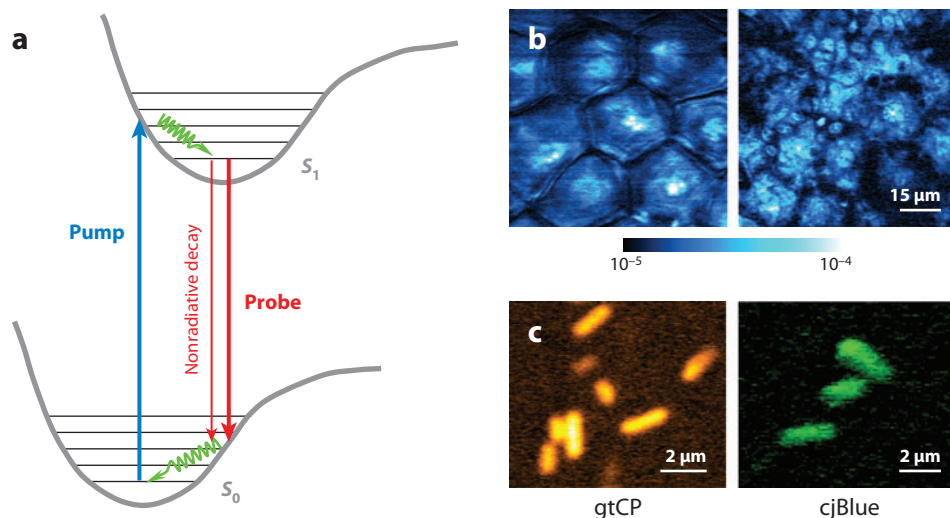


Figure 9

Stimulated emission microscopy. (a) Energy diagram of stimulated emission. (b) A pair of stimulated emission images of toluidine blue O, a drug used as a photosensitizer in photodynamic therapy, at two different z depths (3 and 25 μm , respectively), delivered onto a mouse ear. Optical sectioning is evident. (c) Stimulated emission images of genetically encoded nonfluorescent chromoproteins, gtCP and cjBlue, inside *Escherichia coli* cells that contain corresponding expression plasmids. Panels b and c adapted from Reference 85.

The second example of pump-probe spectroscopy is stimulated emission, which is the working principle for light amplification in the laser. The population-dumping aspect of stimulated emission has been utilized in spectroscopy and microscopy, such as in stimulated emission pumping (82), super-resolution fluorescence microscopy (83), and fluorescence lifetime imaging (84). We recently demonstrated the use of the light-amplification aspect of stimulated emission as a contrast mechanism for highly sensitive imaging of nonfluorescent chromophores (85) (**Figure 9**). Certain chromophores, such as chromoproteins, absorb light intensely but have undetectable fluorescence. This is because their spontaneous emission is dominated by their fast nonradiative decay (which can be four orders of magnitude faster than their rate of spontaneous emission) from the excited state (86). Stimulated emission microscopy exhibits a few advantages over direct one-beam absorption microscopy for imaging those molecules. First, the pump-probe signal is generated only at the laser spot, offering 3D sectioning. Second, the high-frequency modulation transfer scheme provides shot-noise-limited detection sensitivity, whereas one-beam absorption suffers from laser intensity noise at low frequencies. Third, the absorption approach cannot distinguish true optical absorption from light scattering from heterogeneous biological samples, as both effects are manifested as light extinction at the detector. In contrast, stimulated emission microscopy measures the response of the probe beam intensity only at the pump beam modulation frequency, filtering out variations of the probe beam intensity due to sample scattering at low frequencies.

With the introduction of a stimulated emission pulse with appropriate time delay and energy, the chromophore, after being photoexcited to the excited state by a pump pulse, is much more likely to be brought down to the ground state through the radiative decay channel (which consists of spontaneous emission and stimulated emission) than through the nonradiative decay channel. As a result of the new photons radiated by the molecule, the intensity of the stimulation beam is increased concurrently. Although the gain after interaction with the photoexcited chromophores is small, it

Chromoprotein:

protein that contains nonfluorescent pigments and hence is capable of absorbing light

can be extracted by high-frequency demodulation, making the chromophore detectable. We have reached the sensitivity of detecting five molecules in aqueous solution at the laser focus (85).

Finally, modulation transfer microscopy also can be applied to ground-state depletion spectroscopy. Unlike stimulated emission, ground-state depletion employs pump and probe pulses that are both resonant with the absorption band of the chromophore of the ground state (**Figure 10a**). In the absence of the pump pulse, the probe pulse becomes absorbed and attenuated by the chromophores. However, after being excited to the higher electronic state by the pump pulse, the chromophore then absorbs the subsequent probe pulse to a lesser extent because of the

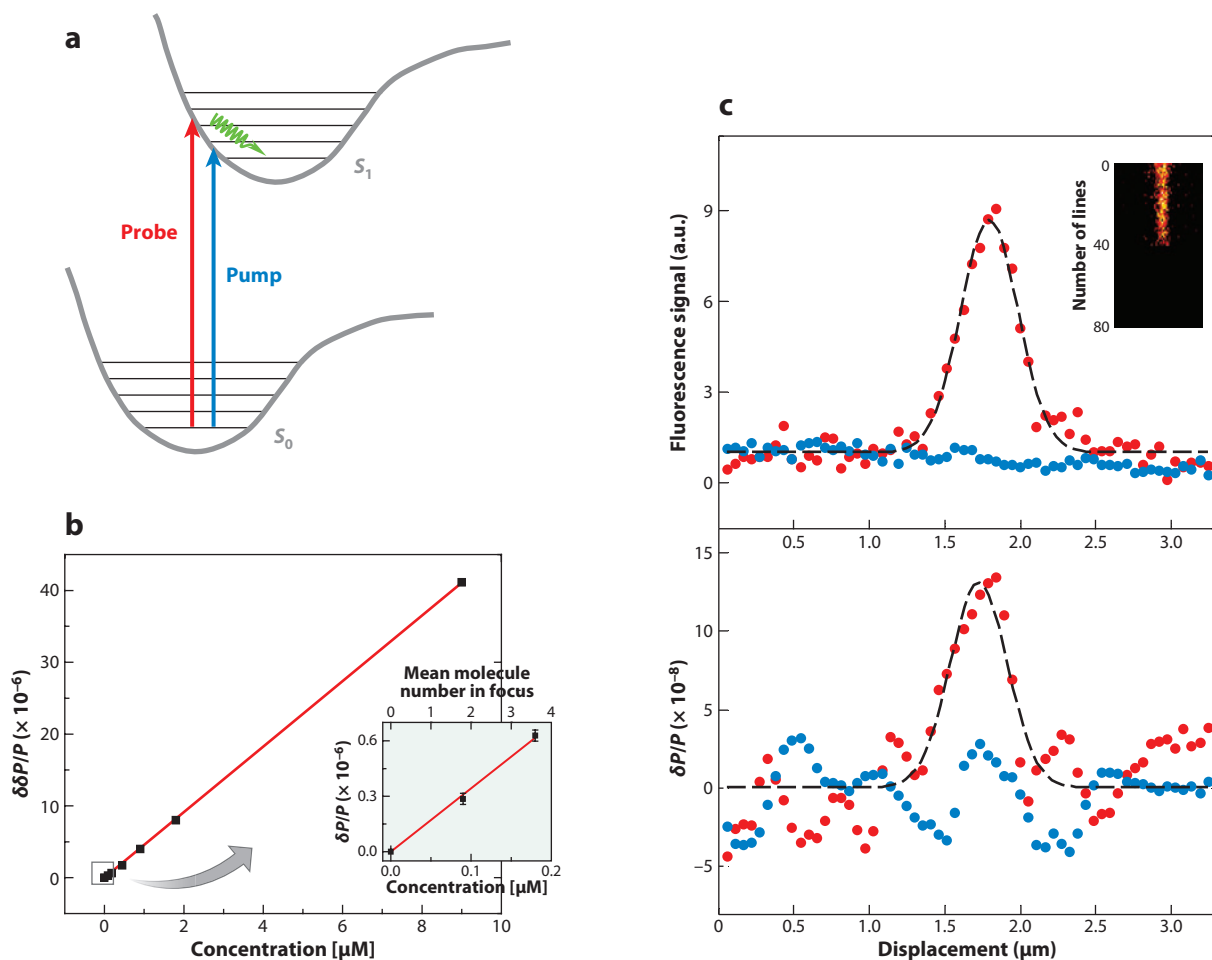


Figure 10

Ground-state depletion microspectroscopy of single molecules. (*a*) Energy diagram of ground-state depletion. (*b*) Ground-state depletion signal as a function of concentration of aqueous Atto647N solution. The inset indicates the data points at the lowest concentrations, with the estimated mean molecule number in the probe volume. Error bars are for 1-s integration time, indicating that single-molecule sensitivity is reachable. (*c*) Simultaneous fluorescence and ground-state depletion line scans for a single Atto647N molecule embedded in PMMA film, averaged before (red) and after (blue) photobleaching. The inset shows the 1D fluorescence image constructed from repeated line scans across the molecule, which underwent abrupt single-step photobleaching after 45 lines. Figure adapted from Reference 87.

transient depletion of the ground-state population. Hence the presence of the pump beam results in a relative gain of the probe beam intensity.

The ground-state depletion effect can also be created by using continuous-wave laser beams under a steady-state condition. Recently, this was employed to detect an absorption signal from single molecules in the condensed phase at room temperature with shot-noise-limited sensitivity (87). As shown in **Figure 10**, the peak value of the ground-state depletion signal from a single Atto647N molecule in PMMA film, $\delta\delta P/P \sim 13.5 \times 10^{-8}$, coincides well with the lateral position of the peak in the simultaneous fluorescence scan. As expected, the average of the scanned lines across the photobleached molecule exhibits no signal.

CONCLUDING REMARKS

Although fluorescence labeling and imaging have become increasingly sophisticated (88–90), many more molecular species cannot or should not be labeled in biomedicine and materials sciences. To this end, coherent nonlinear optical microscopy, especially nonlinear dissipation microscopy and pump-probe microscopy, represents an emerging direction for label-free optical imaging with high sensitivity and specificity. Exciting applications in various areas are expected for many years to come.

SUMMARY POINTS

1. Nonfluorescent molecules can be imaged in three dimensions with high sensitivity and specificity by nonlinear dissipation microscopy and pump-probe microscopy through a modulation transfer scheme.
2. High-frequency modulation, together with the associated phase-sensitive lock-in detection, removes all the low-frequency laser intensity noise and permits shot-noise-limited sensitivity. For biological samples, this avoids the contribution from linear scattering due to heterogeneous refractive index. The ultimate single-molecule sensitivity has been achieved already in a ground-state depletion experiment.
3. Compared with the class of parametric generation microscopy, nonlinear dissipation microscopy and pump-probe microscopy exhibit much improved molecular specificity, by interrogating directly real electronic or vibrational transitions instead of intermediate virtual states.
4. The stimulated coherent excitation of vibrational oscillators by the joint action of pump and Stokes (probe) photons gives rise to a much more efficient vibrational excitation than that of spontaneous Raman microscopy, resulting in orders-of-magnitude improvement in acquisition speed.
5. SRS microscopy overcomes the long-standing difficulty of a nonresonant background in CARS microscopy, by detecting the direct energy transfer from the laser fields to the vibrational states instead of reading out the vibrational coherence. With the removal of such a background, SRS displays a variety of advantages over CARS microscopy, notably, a clean and undistorted spectrum, shot-noise-limited sensitivity, strict linear concentration dependence, and the existence of a well-defined point spread function.

6. Two-photon absorption can be sensitively detected by modulation transfer between two laser beams with two different colors.
7. Optical imaging based on pump-probe spectroscopy, including stimulated emission, excited-state absorption, and ground-state depletion, is capable of imaging nonfluorescent chromophores with superb sensitivity.

FUTURE ISSUES

1. What is the ultimate sensitivity of SRS microscopy? Can special laser excitation sources significantly enhance the coherence amplitude ρ_{vib} ?
2. Can principles (such as entangled photons or squeezed light) and techniques in quantum optics be borrowed to surmount the shot-noise-limited detection sensitivity?
3. Can the modulation of other optical properties (such as frequency, polarization, and phase) of the pump beam bring advantages over intensity modulation?
4. How can we achieve super-resolution (beyond the diffraction-limited resolution) imaging for coherent nonlinear optical microscopy?
5. Can fiber delivery and fiber-based laser sources reduce the cost and complexity of microscopy systems?

DISCLOSURE STATEMENT

Patents and patent applications held by Harvard University have been licensed to multiple microscope manufacturers.

ACKNOWLEDGMENTS

We wish to thank many colleagues and collaborators who have contributed to the development and applications of SRS microscopy, stimulated emission microscopy, and ground-state depletion microscopy, in particular, B.G. Saar, Shasha Chong, G.R. Holtom, M. Roeffaers, X. Zhang, R. Roy, J.C. Tsai, J.X. Kang, M.C. Wang, S.Y. Ding, and G. Ruvkun. This research was supported by grants from the Department of Energy's Basic Energy Sciences program (DE-FG02-07ER15875) and the NSF (grants DBI-0649892 and CHE-0634788), NIH Director's Pioneer Award (to X.S.X.), NIH T-R01 (1R01EB010244-01), the Bill & Melinda Gates Foundation, and Pfizer Global Medical.

LITERATURE CITED

1. Lakowicz JR. 1983. *Principles of Fluorescence Spectroscopy*. New York: Plenum
2. Pawley JB, ed. 2006. *Handbook of Biological Confocal Microscopy*. New York: Springer. 3rd ed.
3. Chalfie M, Tu Y, Euskirchen G, Ward WW, Prasher DC. 1994. Green fluorescent protein as a marker for gene expression. *Science* 263:802–5
4. Tsien RY. 1998. The green fluorescent protein. *Annu. Rev. Biochem.* 67:509–44
5. Zhang J, Campbell RE, Ting AY, Tsien RY. 2002. Creating new fluorescent probes for cell biology. *Nat. Rev. Mol. Biol.* 3:906–18
6. Michalet X, Pinaud FF, Bentolila LA, Tsay JM, Doose S, et al. 2005. Quantum dots for live cells, in vivo imaging, and diagnostics. *Science* 307:538–44

7. Denk W, Strickler J, Webb WW. 1990. Two-photon laser scanning fluorescence microscopy. *Science* 248:73–76
8. Moerner WE, Orrit M. 1999. Illuminating single molecules in condensed matter. *Science* 283:1670–76
9. Xie XS, Trautman JK. 1998. Optical studies of single molecules at room temperature. *Annu. Rev. Phys. Chem.* 49:441–80
10. Hell SW. 2007. Far-field optical nanoscopy. *Science* 316:1153–58
11. Levenson MD, Kano SS. 1988. *Introduction to Nonlinear Laser Spectroscopy*. San Diego: Academic
12. Hellwarth R, Christensen P. 1974. Nonlinear optical microscopic examination of structure in polycrystalline ZnSe. *Opt. Commun.* 12:318–22
13. Sheppard CJR, Kompfner R, Gannaway J, Walsh D. 1977. Scanning harmonic optical microscope. *IEEE J. Quantum Electron.* 13E:D100
14. Nuriya M, Jiang J, Nemet B, Eisenthal KB, Yuste R. 2006. Imaging membrane potential in dendritic spines. *Proc. Natl. Acad. Sci. USA* 103:786–90
15. Barad Y, Eisenberg H, Horowitz M, Silberberg Y. 1997. Nonlinear scanning laser microscopy by third harmonic generation. *Appl. Phys. Lett.* 70:922–24
16. Squier JA, Muller M, Brakenhoff GJ, Wilson KR. 1998. Third harmonic generation microscopy. *Opt. Express* 3:315–24
17. Potma EO, Boeij WPD, Wiersma DA. 2000. Nonlinear coherent four-wave mixing in optical microscopy. *J. Opt. Soc. Am. B* 17:1678–84
18. Min W, Lu S, Rueckel M, Holtom GR, Xie XS. 2009. Near-degenerate four-wave-mixing microscopy. *Nano Lett.* 9:2423–26
19. Kim H, Sheps T, Collins PG, Potma EO. 2009. Nonlinear optical imaging of individual carbon nanotubes with four-wave-mixing microscopy. *Nano Lett.* 9:2991–95
20. Campagnola PJ, Clark HA, Mohler WA, Lewis A, Loew LW. 2003. Second-harmonic imaging microscopy for visualizing biomolecular arrays in cells, tissues and organisms. *Nat. Biotechnol.* 21:1356–60
21. Zipfel WR, Williams RM, Christie R, Nikitin AY, Hyman BT, Webb WW. 2003. Live tissue intrinsic emission microscopy using multiphoton-excited native fluorescence and second harmonic generation. *Proc. Natl. Acad. Sci. USA* 100:7075–80
22. Clark RJH, Hester RE, eds. 1988. *Advances in Nonlinear Spectroscopy*, Vol. 15. New York: Wiley
23. Turrell G, Corset J. 1996. *Raman Microscopy: Developments and Applications*. San Diego: Academic
24. Maker PD, Terhune RW. 1965. Study of optical effects due to an induced polarization third order in the electric field strength. *Phys. Rev.* 137:A801–18
25. Boyd RW. 2003. *Nonlinear Optics*. London: Academic
26. Petrov GI, Arora R, Yakovlev VV, Wang X, Sokolov AV, Scully MO. 2007. Comparison of coherent and spontaneous Raman microspectroscopies for noninvasive detection of single bacterial endospores. *Proc. Natl. Acad. Sci. USA* 104:7776–79
27. Pestov D, Ariunbold GO, Wang X, Murawski RK, Sautenkov VA, et al. 2007. Coherent versus incoherent Raman scattering: molecular coherence excitation and measurement. *Opt. Lett.* 32:1725–27
28. Dogariu A, Goltsov A, Xia H, Scully MO. 2008. Concentration dependence in coherent Raman scattering. *J. Mod. Opt.* 55:3255–61
29. Cheng JX, Xie XS. 2004. Coherent anti-Stokes Raman scattering microscopy: instrumentation, theory, and applications. *J. Phys. Chem. B* 108:827–40
30. Müller M, Zumbusch A. 2007. Coherent anti-Stokes Raman scattering microscopy. *Chemphyschem* 8:2156–70
31. Evans CL, Xie XS. 2008. Coherent anti-Stokes Raman scattering microscopy: chemical imaging for biology and medicine. *Annu. Rev. Anal. Chem.* 1:883–909
32. Duncan MD, Reintjes J, Manuccia TJ. 1982. Scanning coherent anti-Stokes Raman microscope. *Opt. Lett.* 7:350–52
33. Zumbusch A, Holtom GR, Xie XS. 1999. Three-dimensional vibrational imaging by coherent anti-Stokes Raman scattering. *Phys. Rev. Lett.* 82:4142–45
34. Volkmer A, Cheng J, Xie XS. 2001. Vibrational imaging with high sensitivity via epi-detected coherent anti-Stokes Raman scattering microscopy. *Phys. Rev. Lett.* 87:023901

35. Evans CL, Potma EO, Puoris'haag M, Cote D, Lin CP, Xie XS. 2005. Chemical imaging of tissue in vivo with video-rate coherent anti-Stokes Raman scattering microscopy. *Proc. Natl. Acad. Sci. USA* 102:16807–12
36. Nan X, Cheng JX, Xie XS. 2003. Vibrational imaging of lipid droplets in live fibroblast cells with coherent anti-Stokes Raman scattering microscopy. *J. Lipid Res.* 44:2202–8
37. Wang HW, Fu Y, Huff TB, Le TT, Wang H, Cheng JX. 2009. Chasing lipids in health and diseases by coherent anti-Stokes Raman scattering microscopy. *Vib. Spectrosc.* 50:160–67
38. Begin S, Belanger E, Laffray S, Vallee R, Cote D. 2009. In vivo optical monitoring of tissue pathologies and diseases with vibrational contrast. *J. Biophoton.* 2:632–42
39. Enejder A, Brackmann C, Svedberg F. 2010. Coherent anti-Stokes Raman scattering microscopy of cellular lipid storage. *IEEE J. Sel. Top. Quantum Electron.* 16:506–15
40. Le TT, Duren HM, Slipchenko MN, Hu CD, Cheng JX. 2010. Label-free quantitative analysis of lipid metabolism in living *Caenorhabditis elegans*. *J. Lipid Res.* 51:672–77
41. Cheng JX, Book LD, Xie XS. 2001. Polarization coherent anti-Stokes Raman scattering microscopy. *Opt. Lett.* 26:1341–43
42. Lu F, Zheng W, Sheppard C, Huang Z. 2008. Interferometric polarization coherent anti-Stokes Raman scattering (IP-CARS). *Opt. Lett.* 33:602–4
43. Volkmer A, Book LD, Xie XS. 2002. Time-resolved coherent anti-Stokes Raman scattering microscopy: imaging based on Raman free induction decay. *Appl. Phys. Lett.* 80:1505–7
44. Evans CL, Potma EO, Xie XS. 2004. Coherent anti-Stokes Raman scattering interferometry: determination of the real and imaginary components of nonlinear susceptibility $\chi^{(3)}$ for vibrational microscopy. *Opt. Lett.* 29:2923–25
45. Lim SH, Caster AG, Leone SR. 2005. Single-pulse phase-control interferometric coherent anti-Stokes Raman scattering spectroscopy. *Phys. Rev. A* 72:041803
46. Marks DL, Boppart SA. 2004. Nonlinear interferometric vibrational imaging. *Phys. Rev. Lett.* 92:123905
47. Potma EO, Evans CL, Xie XS. 2006. Heterodyne coherent anti-Stokes Raman scattering (CARS) imaging. *Opt. Lett.* 31:241–43
48. von Vacano B, Buckup T, Motzkus M. 2006. Highly sensitive single-beam heterodyne coherent anti-Stokes Raman scattering. *Opt. Lett.* 31:2495–97
49. Jurna M, Korterik JP, Otto C, Herek JL, Offerhaus HL. 2008. Background free CARS imaging by phase sensitive heterodyne CARS. *Opt. Express* 16:15863–69
50. Dudovich N, Oron D, Silberberg Y. 2002. Single-pulse coherently controlled nonlinear Raman spectroscopy and microscopy. *Nature* 418:512–14
51. Lim SH, Caster AG, Nicolet O, Leone SR. 2006. Chemical imaging by single pulse interferometric coherent anti-Stokes Raman scattering microscopy. *J. Phys. Chem. B* 110:5196–204
52. Li H, Ahmadi Harris D, Xu B, Wrzesinski PJ, Lozovoy VV, Dantus M. 2008. Coherent mode-selective Raman excitation towards standoff detection. *Opt. Express* 16:5499–504
53. Silberberg Y. 2009. Quantum coherent control for nonlinear spectroscopy and microscopy. *Annu. Rev. Phys. Chem.* 60:277–92
54. Vartiainen EM, Rinia HA, Müller M, Bonn M. 2006. Direct extraction of Raman line-shapes from congested CARS spectra. *Opt. Express* 14:3622–30
55. Liu Y, Lee YJ, Cicerone MT. 2009. Broadband CARS spectral phase retrieval using a time-domain Kramers–Kronig transform. *Opt. Lett.* 34:1363–65
56. Ganikhanov F, Evans CL, Saar BG, Xie XS. 2006. High sensitivity vibrational imaging with frequency modulation coherent anti-Stokes Raman scattering microscopy. *Opt. Lett.* 31:1872–74
57. Saar BG, Holtom GR, Freudiger CW, Ackermann C, Hill W, Xie XS. 2009. Intracavity wavelength modulation of an optical parametric oscillator for coherent Raman microscopy. *Opt. Express* 17:12532–39
58. Woodbury EJ, Ng WK. 1962. Ruby operation in the near IR. *Proc. Inst. Radio Eng.* 50:2367
59. Jones WJ, Stoicheff BP. 1964. Inverse Raman spectra: induced absorption at optical frequencies. *Phys. Rev. Lett.* 13:657–59
60. Bloembergen N. 1967. The stimulated Raman effect. *Am. J. Phys.* 35:989–1023
61. Owyong A. 1978. Coherent Raman gain spectroscopy using CW laser sources. *IEEE J. Quantum Electron.* QE-14:192–203

62. Levine BF, Shank CV, Heritage JP. 1979. Surface vibrational spectroscopy using stimulated Raman scattering. *IEEE J. Quantum Electron.* QE-15:1418–32
63. Levenson MD, Moerner WE, Horne DE. 1983. FM spectroscopy detection of stimulated Raman gain. *Opt. Lett.* 8:108–10
64. Kukura P, McCamant DW, Mathies RA. 2007. Femtosecond stimulated Raman spectroscopy. *Annu. Rev. Phys. Chem.* 58:461–88
65. Fang C, Frontiera RR, Tran R, Mathies RA. 2009. Mapping GFP structure evolution during proton transfer with femtosecond Raman spectroscopy. *Nature* 462:200–4
66. Ploetz E, Laingruber S, Berner S, Zinth W, Gilch P. 2007. Femtosecond stimulated Raman microscopy. *Appl. Phys. B* 87:389–93
67. Freudiger CW, Min W, Saar BG, Lu S, Holtom GR, et al. 2008. Label-free biomedical imaging with high sensitivity by stimulated Raman scattering microscopy. *Science* 322:1857–61
68. Nandakumar P, Kovalev A, Volkmer A. 2009. Vibrational imaging based on stimulated Raman scattering microscopy. *New J. Phys.* 11:033026–35
69. Ozeki Y, Dake F, Kajiyama S, Fukui K, Itoh K. 2009. Analysis and experimental assessment of the sensitivity of stimulated Raman scattering microscopy. *Opt. Express* 17:3651–58
70. Saar BG, Freudiger CW, Reichman J, Stanley CM, Holtom GR, Xie XS. 2010. Video-rate molecular imaging in vivo with stimulated Raman scattering. *Science* 330:1368–71
71. Freudiger CW, Saar BG, Xie XS, Kesari S, Young GS. 2010. Stain-free histopathology with coherent Raman imaging. *Nature*. Manuscript submitted
72. Roeffaers MJB, Zhang X, Freudiger CW, Saar BG, van Ruijven M, et al. 2010. Label-free imaging of biomolecules in food products using stimulated Raman microscopy. *J. Biomed. Opt.* 15:066016
73. Saar BG, Zeng Y, Freudiger CW, Liu YS, Himmel ME, et al. 2010. Label-free, real-time monitoring of biomass processing with stimulated Raman scattering microscopy. *Angew. Chem. Int. Ed. Engl.* 49:5476–79
74. Wang MC, Min W, Freudiger CW, Ruvkun G, Xie XS. 2011. RNA interference screening for fat regulatory genes with stimulated Raman scattering microscopy. *Nat. Methods*. In press
75. Freudiger CW, Min W, Holtom GR, Xu B, Dantus M, Xie XS. 2011. Highly specific label-free molecular imaging with spectrally tailored excitation stimulated Raman scattering (STE-SRS) microscopy. *Nat. Photonics*. In press
76. Goeppert-Mayer M. 1931. Über Elementarakte mit zwei Quantensprüngen. *Ann. Phys.* 9:273–95
77. Warren WS, Fischer MC, Ye T. 2007. Novel nonlinear contrast improves deep-tissue microscopy. *Laser Focus World* 43:99–103
78. Ye T, Fu D, Warren WS. 2009. Nonlinear absorption microscopy. *Photochem. Photobiol.* 85:631–45
79. Fu D, Ye T, Matthews TE, Chen BJ, Yurtsever G, Warren WS. 2007. High-resolution in vivo imaging of blood vessels without labeling. *Opt. Lett.* 32:2641–43
80. Fu D, Ye T, Matthews TE, Yurtsever G, Warren WS. 2007. Two-color, two-photon, and excited-state absorption microscopy. *J. Biomed. Opt.* 12:054004
81. Fu D, Matthews TE, Ye T, Piletic IR, Warren WS. 2008. Label-free in vivo optical imaging of microvasculature and oxygenation level. *J. Biomed. Opt.* 13:040503
82. Hamilton CE, Kinsey JL, Field RW. 1986. Stimulated emission pumping: new methods in spectroscopy and molecular dynamics. *Annu. Rev. Phys. Chem.* 37:493–524
83. Hell SW, Wichmann J. 1994. Breaking the diffraction resolution limit by stimulated emission: stimulated-emission-depletion fluorescence microscopy. *Opt. Lett.* 19:780–82
84. Dong CY, So PT, French T, Gratton E. 1995. Fluorescence lifetime imaging by asynchronous pump-probe microscopy. *Biophys. J.* 69:2234–42
85. Min W, Lu S, Chong S, Roy R, Holtom GR, Xie XS. 2009. Imaging chromophores with undetectable fluorescence by stimulated emission microscopy. *Nature* 461:1105–9
86. Turro NJ. 1991. *Modern Molecular Photochemistry*. Mill Valley, CA: Univ. Sci. Books
87. Chong S, Min W, Xie XS. 2010. Ground state depletion microscopy: detection sensitivity of single-molecule optical absorption at room temperature. *J. Phys. Chem. Lett.* 1:3316–22

88. Miller LW, Cornish VW. 2005. Selective chemical labeling of proteins in living cells. *Curr. Opin. Chem. Biol.* 9:56–61
89. Lin MZ, Wang L. 2008. Selective labeling of proteins with chemical probes in living cells. *Physiology* 23:131–41
90. Fernandez-Suarez M, Ting AY. 2008. Fluorescent probes for super-resolution imaging in living cells. *Nat. Rev. Mol. Cell. Biol.* 9:929–43



Contents

Laboring in the Vineyard of Physical Chemistry <i>Benjamin Widom</i>	1
The Ultrafast Pathway of Photon-Induced Electrocyclic Ring-Opening Reactions: The Case of 1,3-Cyclohexadiene <i>Sanghamitra Deb and Peter M. Weber</i>	19
Coarse-Grained (Multiscale) Simulations in Studies of Biophysical and Chemical Systems <i>Shina C.L. Kamerlin, Spyridon Vicatos, Anatoly Dryga, and Arie Warshel</i>	41
Dynamics of Nanoconfined Supercooled Liquids <i>R. Richert</i>	65
Ionic Liquids: Structure and Photochemical Reactions <i>Edward W. Castner Jr., Claudio J. Margulis, Mark Maroncelli, and James F. Wishart</i>	85
Theoretical Study of Negative Molecular Ions <i>Jack Simons</i>	107
Theoretical and Computational Protein Design <i>Ilan Samish, Christopher M. MacDermaid, Jose Manuel Perez-Aguilar, and Jeffery G. Saven</i>	129
Melting and Freezing of Metal Clusters <i>Andrés Aguado and Martin F. Jarrold</i>	151
Astronomical Chemistry <i>William Klemperer</i>	173
Simulating Chemistry Using Quantum Computers <i>Ivan Kassal, James D. Whitfield, Alejandro Perdomo-Ortiz, Man-Hong Yung, and Alán Aspuru-Guzik</i>	185
Multiresonant Coherent Multidimensional Spectroscopy <i>John C. Wright</i>	209
Probing Free-Energy Surfaces with Differential Scanning Calorimetry <i>Jose M. Sanchez-Ruiz</i>	231

Role of Solvation Effects in Protein Denaturation: From Thermodynamics to Single Molecules and Back <i>Jeremy L. England and Gilad Haran</i>	257
Solid-State NMR Studies of Amyloid Fibril Structure <i>Robert Tycko</i>	279
Cooperativity, Local-Nonlocal Coupling, and Nonnative Interactions: Principles of Protein Folding from Coarse-Grained Models <i>Hue Sun Chan, Zhuqing Zhang, Stefan Wallin, and Zhirong Liu</i>	301
Hydrated Acid Clusters <i>Kenneth R. Leopold</i>	327
Developments in Laboratory Studies of Gas-Phase Reactions for Atmospheric Chemistry with Applications to Isoprene Oxidation and Carbonyl Chemistry <i>Paul W. Seakins and Mark A. Blitz</i>	351
Bonding in Beryllium Clusters <i>Michael C. Heaven, Jeremy M. Merritt, and Vladimir E. Bondybey</i>	375
Reorientation and Allied Dynamics in Water and Aqueous Solutions <i>Damien Laage, Guillaume Stirnemann, Fabio Sterpone, Rossend Rey, and James T. Hynes</i>	395
Detecting Nanodomains in Living Cell Membrane by Fluorescence Correlation Spectroscopy <i>Hai-Tao He and Didier Marguet</i>	417
Toward a Molecular Theory of Early and Late Events in Monomer to Amyloid Fibril Formation <i>John E. Straub and D. Thirumalai</i>	437
The Density Matrix Renormalization Group in Quantum Chemistry <i>Garnet Kin-Lic Chan and Sandeep Sharma</i>	465
Thermodynamics and Mechanics of Membrane Curvature Generation and Sensing by Proteins and Lipids <i>Tobias Baumgart, Benjamin R. Capraro, Chen Zbu, and Sovan L. Das</i>	483
Coherent Nonlinear Optical Imaging: Beyond Fluorescence Microscopy <i>Wei Min, Christian W. Freudiger, Sijia Lu, and X. Sunney Xie</i>	507
Roaming Radicals <i>Joel M. Bowman and Benjamin C. Shepler</i>	531
Coarse-Grained Simulations of Macromolecules: From DNA to Nanocomposites <i>Juan J. de Pablo</i>	555

New Developments in the Physical Chemistry of Shock Compression <i>Dana D. Dlott</i>	575
Solvation Dynamics and Proton Transfer in Nanoconfined Liquids <i>Ward H. Thompson</i>	599
Nonadiabatic Events and Conical Intersections <i>Spiridoula Matsika and Pascal Krause</i>	621
Lessons in Fluctuation Correlation Spectroscopy <i>Michelle A. Digman and Enrico Gratton</i>	645

Indexes

Cumulative Index of Contributing Authors, Volumes 58–62	669
Cumulative Index of Chapter Titles, Volumes 58–62	672

Errata

An online log of corrections to *Annual Review of Physical Chemistry* articles may be found at <http://physchem.annualreviews.org/errata.shtml>



ANNUAL REVIEWS

It's about time. Your time. It's time well spent.

New From Annual Reviews:

Annual Review of Statistics and Its Application

Volume 1 • Online January 2014 • <http://statistics.annualreviews.org>

Editor: **Stephen E. Fienberg**, *Carnegie Mellon University*

Associate Editors: **Nancy Reid**, *University of Toronto*

Stephen M. Stigler, *University of Chicago*

The *Annual Review of Statistics and Its Application* aims to inform statisticians and quantitative methodologists, as well as all scientists and users of statistics about major methodological advances and the computational tools that allow for their implementation. It will include developments in the field of statistics, including theoretical statistical underpinnings of new methodology, as well as developments in specific application domains such as biostatistics and bioinformatics, economics, machine learning, psychology, sociology, and aspects of the physical sciences.

Complimentary online access to the first volume will be available until January 2015.

TABLE OF CONTENTS:

- *What Is Statistics?* Stephen E. Fienberg
- *A Systematic Statistical Approach to Evaluating Evidence from Observational Studies*, David Madigan, Paul E. Stang, Jesse A. Berlin, Martijn Schuemie, J. Marc Overhage, Marc A. Suchard, Bill Dumouchel, Abraham G. Hartzema, Patrick B. Ryan
- *The Role of Statistics in the Discovery of a Higgs Boson*, David A. van Dyk
- *Brain Imaging Analysis*, F. DuBois Bowman
- *Statistics and Climate*, Peter Guttorp
- *Climate Simulators and Climate Projections*, Jonathan Rougier, Michael Goldstein
- *Probabilistic Forecasting*, Tilmann Gneiting, Matthias Katzfuss
- *Bayesian Computational Tools*, Christian P. Robert
- *Bayesian Computation Via Markov Chain Monte Carlo*, Radu V. Craiu, Jeffrey S. Rosenthal
- *Build, Compute, Critique, Repeat: Data Analysis with Latent Variable Models*, David M. Blei
- *Structured Regularizers for High-Dimensional Problems: Statistical and Computational Issues*, Martin J. Wainwright
- *High-Dimensional Statistics with a View Toward Applications in Biology*, Peter Bühlmann, Markus Kalisch, Lukas Meier
- *Next-Generation Statistical Genetics: Modeling, Penalization, and Optimization in High-Dimensional Data*, Kenneth Lange, Jeanette C. Papp, Janet S. Sinsheimer, Eric M. Sobel
- *Breaking Bad: Two Decades of Life-Course Data Analysis in Criminology, Developmental Psychology, and Beyond*, Elena A. Erosheva, Ross L. Matsueda, Donatello Telesca
- *Event History Analysis*, Niels Keiding
- *Statistical Evaluation of Forensic DNA Profile Evidence*, Christopher D. Steele, David J. Balding
- *Using League Table Rankings in Public Policy Formation: Statistical Issues*, Harvey Goldstein
- *Statistical Ecology*, Ruth King
- *Estimating the Number of Species in Microbial Diversity Studies*, John Bunge, Amy Willis, Fiona Walsh
- *Dynamic Treatment Regimes*, Bibhas Chakraborty, Susan A. Murphy
- *Statistics and Related Topics in Single-Molecule Biophysics*, Hong Qian, S.C. Kou
- *Statistics and Quantitative Risk Management for Banking and Insurance*, Paul Embrechts, Marius Hofert

Access this and all other Annual Reviews journals via your institution at www.annualreviews.org.

ANNUAL REVIEWS | Connect With Our Experts

Tel: 800.523.8635 (US/CAN) | Tel: 650.493.4400 | Fax: 650.424.0910 | Email: service@annualreviews.org

